Journal of Molecular Structure 1381 (2027) 147455

Contents lists available at ScienceDirect

Journal of Molecular Structure

journal homepage: www.elsevier.com/locate/molstr

Synthesis, crystal structure, DFT, and molecular docking studies of quinazoline-based ML-167 derivatives

Sajda Ashraf [a], Shabnam Alizadeh [a], Issam Ameziane El Hassani [a], Aybuke Ozturk [a], Naime Ceren Suer [a], Woonghee Kim [b], Gonca Candan [a], Gizem Batı Ayaz [a], Murat Ozdemir [a], Güldeniz Yeşilyurt [a], Essam Hanashalshahaby [a], Hasan Turkez [c], Adil Mardinoglu [a,b,c,d,*]

[a] Trustlife Labs, Drug Research & Development Center, Istanbul, 34774, Turkey
[b] Science for Life Laboratory, KTH-Royal Institute of Technology, Stockholm, SE-17165, Sweden
[c] Department of Medical Biology, Faculty of Medicine, Atatürk University, Erzurum, Turkey
[d] Centre for Host-Microbiome Interactions, Faculty of Dentistry, Oral & Craniofacial Sciences, King's College London, SE1 9RT, London, United Kingdom

ARTICLE INFO

Keywords:
Sarcopenia
quinazoline
ML-167
C2C12
DFT
X-ray crystallography

ABSTRACT

Sarcopenia is a chronic disease characterized by loss of skeletal muscle mass and strength, posing a rising societal health challenge among the elderly, leading to increased risks of disability, fractures, falls, and mortality. Despite its clinical significance, there are currently no approved medicinal interventions for this condition. In this study, we used a systems biology framework to uncover potential therapeutic targets for sarcopenia. Based on computational analysis, CYC1 was identified as a key druggable protein. Following bioinformatic screening, ML-167 was selected as a candidate for repurposing. Guided by this insight, we have rationally designed and synthesized a novel series of ML-167-based derivatives, intending to modulate CYC1 activity. For structural validations, comprehensive spectroscopic techniques, including ^{1}H and ^{13}C NMR, MS, and, where applicable, single-crystal X-ray crystallography techniques were used. In vitro evaluation of the ML-167 derivatives in C2C12 cells established structure-dependent effects on cell viability. Several derivatives exhibited proliferation levels similar to the control group and indicate differences in biological activity among the derivatives. Computational studies, including molecular docking, density functional theory (DFT) calculations, and analyses of frontier molecular orbitals (FMOs), disclosed favorable electronic features, charge-transfer characteristics, and binding interactions with CYC1. Noncovalent interaction (NCI), reduced density gradient (RDG), electron localization function (ELF), and quantum theory of atoms in molecules (QTAIM) analyses highlighted the role of dispersive forces and hydrogen bonding in stabilizing the ligand-protein complex. Structure–activity relationship (SAR) analysis and in vitro cell proliferation assays identified compounds 3a, 3f, and 5a as the most promising leads, demonstrating optimal binding profiles and favorable biological activity.

1. Introduction

Sarcopenia is a chronic muscle disease characterized by progressive loss of muscle mass, strength, and function, causing a substantial health risk to the elderly worldwide [1]. Although sarcopenia is common among older adults, its onset can begin as early as midlife [2] and is often exacerbated in people with chronic diseases, including cancer [3], chronic kidney disease [4], Parkinson disease [5], liver dysfunction [6], and metabolic disorders [7]. With the aging population increasing, it's urgent to find new drug targets and develop effective treatments [1].

Despite considerable efforts, sarcopenia is still not fully understood. Challenges include the lack of suitable animal models and the difficulty in distinguishing "pure sarcopenia" from other age-related health problems [8,9]. The lack of agreement made regulators hesitant to recognize sarcopenia as a curable condition, which has slowed the development of potential therapies [10].

Quinazoline scaffolds represent an important class of biologically active nitrogen heterocyclic compounds, and have gathered substantial attention in the development of drug design due to their wide-range pharmacological effects [11]. Investigation of this scaffold began with the discovery of febrifugine, a quinazolinone-based alkaloid with potential antimalarial activity, isolated from the Chinese plant Dichroa

* Corresponding author at:KTH Royal Institute of Technology, Sweden.
E-mail address: adilm@scilifelab.se (A. Mardinoglu).

https://doi.org/10.1016/j.molstruc.2026.147455
Received 30 June 2026; Received in revised form 18 August 2026; Accepted 24 August 2026
Available online 26 August 2026

febrifuga Lour [12] In addition to its antimalarial properties, quinazoline derivatives exhibit a variety of biological activities, including anticancer, anti-inflammatory, antibacterial, and antihypertensive effects [13].

Our previous findings indicated that C2C12 myoblasts serve as a reliable in vitro model for assessing the biological effects of the synthesized compounds [14]. The design and synthesis of these compounds were centred on ML-167 using a drug repurposing strategy (Fig. 1). Structural characterization of the compounds was performed using ^{1}H and ^{13}C NMR spectroscopy as well as mass spectrometry to verify their chemical structures. Additionally, the structure of compound 583 was determined and confirmed by X-ray crystallography analysis. For the in vitro evaluation of muscle cell viability and proliferation, the MTT assay was performed in C2C12 cells. This assay was performed to assess the proliferative or cytotoxic effects of the compounds and their impact on muscle cell growth. To further understand how structural variation affects biological activity, Structure Activity Relationship (SAR) analysis, alongside molecular docking and computational quantum mechanics approaches, provides detail understanding of the structural features governing biological activity and enhances the compounds' effectiveness.

2. Experiments

2.1. Chemistry

2.1.1. General Methods

All materials and solvents were obtained from commercial suppliers and used without further purification. Microwave-assisted reactions were performed using a Discover 2.0 Initiator microwave synthesis system. Reaction progress was monitored by liquid chromatography–mass spectrometry (LC–MS), utilizing a Thermo Fisher TSQ Series instrument equipped with an Athena C18-WP column (100 Å, 2.1 × 50 mm, 3 μm) and a mobile phase consisting of water/methanol with 0.01% formic acid. Alternatively, reaction monitoring was conducted using thin-layer chromatography (TLC) on silica gel precoated aluminum plates (Kieselgel 60, F254, E. Merck, Darmstadt, 64293, Germany). Chromatographic separations and detection were visualized under UV light at 254 and 366 nm. Compounds were purified by a PuriFlash XS 520 Plus system (Interchim), equipped with an integrated UV detector, evaporative light scattering detector (ELSD), and fraction collector, using Interchim silica gel columns.^{1}H NMR spectra were obtained using a Bruker Avance 500 MHz spectrometer with DMSO-d_6 as the solvent. ^{13}C NMR spectra were recorded at 126 MHz on a Bruker instrument using deuterated solvents, with the central peak of the solvent serving as the internal reference. Chemical shifts (δ) are reported in parts per million (ppm) relative to tetramethylsilane (TMS).

2.1.2. General Synthesis of ML-167 derivatives 3a-3c

A mixture of 4,7-dichloroquinazoline **1** (1 mmol, 1 equiv), the appropriate boronic acid **2** (1 mmol, 1 equiv), cesium carbonate Cs_2CO_3 (2 mmol, 2 equiv), and Pd(dppf)Cl_2 catalyst (0.2 mmol, 0.2 equiv) was combined in tetrahydrofuran (THF, 3 mL) within a 30 mL Pyrex microwave reaction tube. The reaction mixture was stirred under a nitrogen atmosphere at room temperature for 10 minutes, followed by heating at 160°C for 10 minutes. Upon completion, the mixture was allowed to cool to ambient temperature and subsequently extracted with chloroform (30 mL). The combined organic layers were dried over anhydrous magnesium sulfate ($MgSO_4$), concentrated under reduced pressure, and the crude product was purified by flash chromatography using a hexane: ethyl acetate (1:1) solvent system.

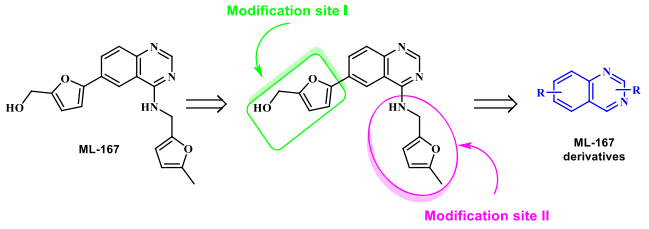

Fig. 1. Rational design of ML-167.

Synthesis of (5-(4-chloroquinazolin-7-yl)furan-2-yl)methanol 3a

White solid, Yield: 78%, ^{1}H NMR (500 MHz, DMSO-d_6) δ 9.23 (s, 1H), 8.94 (d, J = 9.1 Hz, 1H), 8.09 (d, J = 2.2 Hz, 1H), 7.82 (dd, J = 9.1, 2.3 Hz, 1H), 7.64 (d, J = 3.5 Hz, 1H), 6.70 (d, J = 3.5 Hz, 1H), 5.61 (t, J = 6.0 Hz, 1H), 4.63 (d, J = 5.8 Hz, 2H). ^{13}C NMR (126 MHz, DMSO-d6) δ 161.16, 155.91, 154.64, 152.31, 151.79, 139.34, 129.48, 129.20, 127.71, 118.97, 118.62, 110.44, 56.44. (ESI-MS): m/z 261.0 $[M+H]^+$.

Synthesis of 7-chloro-4-(3,5-dimethoxyphenyl)quinazoline 3b

White solid, Yield: 72%, ^{1}H NMR (500 MHz, DMSO-d_6) δ 9.37 (s, 1H), 8.19 (d, J = 2.2 Hz, 1H), 8.16 (d, J = 9.0 Hz, 1H), 7.78 (dd, J = 9.0, 2.2 Hz, 1H), 6.89 (d, J = 2.3 Hz, 2H), 6.77 (t, J = 2.3 Hz, 1H), 3.83 (s, 7H). ^{13}C NMR (126 MHz, DMSO-d_6) δ 168.13, 160.94, 155.85, 151.49, 139.45, 138.61, 129.69, 129.51, 127.57, 121.54, 108.36, 102.49, 55.98. (ESI-MS): m/z 301.03 $[M+H]^+$.

Synthesis of 7-chloro-4-(4-(trifluoromethyl)phenyl)quinazoline 3c

Cream solid, Yield: 75%, ^{1}H NMR (500 MHz, DMSO-d_6) δ 9.43 (s, 1H), 8.23 (d, J = 2.1 Hz, 1H), 8.08 (d, J = 9.0 Hz, 1H), 8.05 – 7.98 (m, 4H), 7.79 (dd, J = 9.0, 2.2 Hz, 1H). ^{13}C NMR (126 MHz, DMSO-d_6) δ 166.97, 155.89, 151.52, 140.67, 139.69, 131.29, 131.20, 130.95, 130.69, 130.44, 129.79, 129.35, 127.73, 126.12, 126.09, 126.06, 126.03, 125.61, 123.44, 121.46. (ESI-MS): m/z 309.0 $[M+H]^+$.

2.1.3. General Synthesis of ML-167 derivatives 3d-3h

Into the RBF (10 mL), an appropriate intermediate (3a-3c) (0.5 mmol, 1eq) and an appropriate boronic acid 2 (1 mmol, 2eq), Cs2CO3 (2 mmol, 4eq), Pd(dppf)Cl2 catalyst (0,2 mmol, 0.1eq), and THF (3 mL) were introduced into a pyrex MW tube (30 mL) and then H2O (1 mL) was added. The resulting mixture was heated at 160°C for 10 minutes. The mixture was cooled to an ambient temperature and extracted with chloroform (30 mL). After drying over MgSO4, the organic phase was evaporated and the residue was purified by flash chromatography (Hexane: Ethyl Acetate/ 1:1).

Synthesis of (quinazoline-4,7-diylbis(furan-5,2-diyl))dimethanol 3d

White solid, Yield: 70%, ^{1}H NMR (500 MHz, DMSO-d_6) δ 9.19 (s, 1H), 8.92 (d, J = 9.0 Hz, 1H), 8.17 (d, J = 1.8 Hz, 1H), 8.11 (dd, J = 9.0, 1.9 Hz, 1H), 7.60 (d, J = 3.5 Hz, 1H), 7.34 (d, J = 3.4 Hz, 1H), 6.68 (d, J = 3.4 Hz, 1H), 6.55 (d, J = 3.3 Hz, 1H), 5.59 (t, J = 5.9 Hz, 1H), 5.43 (t, J = 5.9 Hz, 1H), 4.64 (d, J = 5.4 Hz, 2H), 4.54 (d, J = 5.3 Hz, 2H). ^{13}C NMR (126 MHz, DMSO-d_6) δ 160.70, 158.12, 155.64, 154.13, 152.32, 151.99, 151.04, 135.39, 127.77, 124.65, 120.99, 119.30, 117.98, 111.44, 110.31, 110.29, 56.47, 56.29. (ESI-MS): m/z 323.01 $[M+H]^+$.

Synthesis of 4,7-bis(3,5-dimethoxyphenyl)quinazoline 3e

White solid, Yield: 68%, ^{1}H NMR (500 MHz, DMSO-d_6) δ 9.36 (s, 1H), 8.36 (d, J = 1.8 Hz, 1H), 8.18 (d, J = 8.7 Hz, 1H), 8.08 (dd, J = 8.8, 1.9 Hz, 1H), 7.02 (d, J = 2.2 Hz, 2H), 6.92 (d, J = 2.3 Hz, 2H), 6.77 (t, J = 2.3 Hz, 1H), 6.63 (t, J = 2.2 Hz, 1H), 3.86 (s, 6H), 3.85 (s, 6H). ^{13}C NMR (126 MHz, DMSO-d_6) δ 167.63, 161.54, 160.93, 155.27, 151.30, 145.86, 140.94, 139.00, 128.09, 127.86, 125.92, 122.04, 108.32, 105.99, 102.35, 101.28, 55.98, 55.91. (ESI-MS): m/z 403.13 $[M+H]^+$.

Synthesis of 4,7-bis(4-(trifluoromethyl)phenyl)quinazoline 3f

Cream solid, Yield: 66%, ^{1}H NMR (500 MHz, DMSO-d_6) δ 9.45 (s, 1H), 8.46 (d, J = 1.7 Hz, 1H), 8.19 – 8.09 (m, 4H), 8.06 (d, J = 8.2 Hz, 2H), 8.02 (d, J = 8.2 Hz, 2H), 7.93 (s, 1H), 7.91 (s, 1H). ^{13}C NMR (126 MHz, DMSO-d_6) δ 166.62, 155.48, 151.27, 144.48, 142.65, 140.92, 131.25, 131.12, 130.86, 130.61, 129.74, 129.48, 128.90, 128.12, 127.96, 126.75, 126.57, 126.54, 126.51, 126.48, 126.10, 126.07,

126.04, 126.01, 125.75, 125.64, 123.59, 123.47, 122.20. (ESI-MS): *m/z* 419.04 $[M+H]^+$.

Synthesis of 7-(3,5-dimethoxyphenyl)-4-(4-(trifluoromethyl) phenyl)quinazoline 3g

White solid, Yield: 73%, ^{1}H NMR (500 MHz, DMSO-d_6) δ 9.42 (s, 1H), 8.40 (t, *J* = 1.3 Hz, 1H), 8.09 (d, *J* = 1.3 Hz, 2H), 8.07 – 8.00 (m, 4H), 7.02 (d, *J* = 2.2 Hz, 2H), 6.63 (t, *J* = 2.2 Hz, 1H), 3.86 (s, 6H). ^{13}C NMR (126 MHz, DMSO-d_6) δ 166.41, 161.55, 155.32, 151.35, 146.08, 141.03, 140.81, 131.24, 130.81, 130.56, 128.40, 127.50, 126.08, 126.05, 126.02, 125.99, 125.65, 123.49, 121.92, 106.05, 101.29, 55.91. (ESI-MS): *m/z* 410.99 $[M+H]^+$.

Synthesis of 3-(4-(4-(trifluoromethyl)phenyl)quinazolin-7-yl) phenol 3h

Cream solid, Yield: 59%, ^{1}H NMR (500 MHz, DMSO-d_6) δ 9.74 (s, 1H), 9.42 (s, 1H), 8.28 (d, *J* = 1.9 Hz, 1H), 8.12 (d, *J* = 8.7 Hz, 1H), 8.08 – 8.03 (m, 4H), 8.02 (d, *J* = 8.3 Hz, 1H), 7.37 (t, *J* = 7.8 Hz, 1H), 7.32 (dt, *J* = 7.7, 1.4 Hz, 1H), 7.25 (t, *J* = 2.1 Hz, 1H), 6.94 – 6.88 (m, 1H). ^{13}C NMR (126 MHz, DMSO-d_6) δ 166.46, 158.57, 155.35, 151.38, 146.33, 141.08, 140.07, 131.23, 130.87, 130.79, 130.54, 128.23, 127.83, 127.69, 126.09, 126.06, 126.03, 126.00, 125.66, 125.58, 123.50, 121.83, 118.68, 116.51, 114.57. (ESI-MS): *m/z* 366.87 $[M+H]^+$.

2.1.4. General synthesis of ML-167 derivatives 5a-5b

A mixture of 4,7-dichloroquinazoline **1** (1 mmol, 1 equiv), (5-methylfuran-2-yl)methanamine **4** (2 mmol, 2 equiv), Cs_2CO_3 (2 mmol, 2 equiv), and Pd(dppf)Cl_2 catalyst (0.2 mmol, 0.2 equiv) was combined in tetrahydrofuran (THF, 3 mL) within a 30 mL Pyrex microwave reaction tube. The reaction mixture was stirred under a nitrogen atmosphere at room temperature for 10 minutes, followed by heating at 160°C for 10 minutes. When an excess of (5-methylfuran-2-yl)methanamine was used, bis-substituted compounds **5b** were generated. Upon completion, the mixture was allowed to cool to ambient temperature and subsequently extracted with chloroform (30 mL). The combined organic layers were dried over anhydrous magnesium sulfate ($MgSO_4$), concentrated under reduced pressure, and the crude product was purified by flash chromatography using a hexane:ethyl acetate (1:1) solvent system.

Synthesis of 7-chloro-*N*-((5-methylfuran-2-yl)methyl)quinazolin-4-amine 5a

Cream solid, Yield: 62%, ^{1}H NMR (500 MHz, DMSO-d_6) δ 8.85 (t, *J* = 5.6 Hz, 1H), 8.51 (s, 1H), 8.34 (d, *J* = 8.9 Hz, 1H), 7.75 – 7.71 (m, 1H), 7.57 (dd, *J* = 8.8, 2.2 Hz, 1H), 6.20 (d, *J* = 3.0 Hz, 1H), 5.99 (dd, *J* = 3.0, 1.2 Hz, 1H), 4.70 (d, *J* = 5.5 Hz, 2H), 2.23 (s, 3H). ^{13}C NMR (126 MHz, DMSO-d_6) δ 167.39, 159.46, 156.62, 150.48, 137.74, 131.98, 129.13, 126.78, 125.60, 114.04, 108.69, 106.92, 37.64, 14.34. (ESI-MS): *m/z* 274.0 $[M+H]^+$.

Synthesis of N^4,N^7-bis((5-methylfuran-2-yl)methyl)quinazoline-4,7-diamine 5b

White solid, Yield: 57%, ^{1}H NMR (500 MHz, DMSO-d_6) δ 8.45 (t, *J* = 5.7 Hz, 1H), 8.42 (s, 1H), 7.36 (dd, *J* = 8.5, 1.1 Hz, 1H), 7.24 (t, *J* = 8.0 Hz, 1H), 6.81 (dd, *J* = 7.8, 1.0 Hz, 1H), 6.52 (t, *J* = 6.2 Hz, 1H), 6.17 (d, *J* = 3.0 Hz, 1H), 6.14 (d, *J* = 3.0 Hz, 1H), 5.96 (dt, *J* = 2.9, 1.3 Hz, 2H), 4.68 (d, *J* = 5.6 Hz, 2H), 4.38 (d, *J* = 6.1 Hz, 2H), 2.21 (s, 6H). ^{13}C NMR (126 MHz, DMSO-d_6) δ 158.85, 152.31, 150.63, 150.52, 150.42, 150.32, 143.11, 138.04, 126.18, 114.29, 107.93, 107.84, 107.72, 107.64, 106.23, 106.14, 36.97, 13.14. (ESI-MS): *m/z* 349.01 $[M+H]^+$.

2.1.5. General synthesis of ML-167 derivatives 5c-5e

Into the RBF (10 mL), an appropriate intermediate (**5a-5b**) (0.5 mmol, 1eq) and an appropriate boronic acid **2** (1 mmol, 2eq), Cs_2CO_3 (2 mmol, 4eq), Pd(dppf)Cl_2 catalyst (0,2 mmol, 0.1eq), and THF (3 mL) were introduced into a pyrex MW tube (30 mL) and then H_2O (1 mL) was added. The resulting mixture was heated at 160°C for 10 minutes. The mixture was cooled to an ambient temperature and extracted with chloroform (30 mL). After drying over $MgSO_4$, the organic phase was evaporated, and the residue was purified by flash chromatography (Hexane: Ethyl Acetate/ 1:1).

Synthesis of *N*-((5-methylfuran-2-yl)methyl)-7-(4-(trifluoromethyl)phenyl)quinazolin-4-amine 5c

White solid, Yield: 54%, ^{1}H NMR (500 MHz, DMSO-d_6) δ 8.82 (t, *J* = 5.6 Hz, 1H), 8.55 (s, 1H), 8.44 (d, *J* = 8.6 Hz, 1H), 8.08 (d, *J* = 8.1 Hz, 2H), 8.04 (d, *J* = 1.9 Hz, 1H), 7.92 (dd, *J* = 8.6, 2.0 Hz, 1H), 7.88 (d, *J* = 8.2 Hz, 2H), 6.21 (d, *J* = 3.1 Hz, 1H), 6.00 (d, *J* = 3.0 Hz, 1H), 4.73 (d, *J* = 5.5 Hz, 2H), 2.24 (s, 3H). ^{13}C NMR (126 MHz, DMSO-d_6) δ 167.39, 159.50, 156.10, 151.15, 150.71, 150.11, 143.39, 142.92, 131.98, 129.13, 128.57, 126.42, 126.39, 126.36, 126.33, 125.94, 125.12, 124.34, 116.16, 115.04, 108.55, 106.92, 97.63, 37.66, 13.79. (ESI-MS): *m/z* 384.0 $[M+H]^+$.

Synthesis of 7-(3,5-dimethoxyphenyl)-*N*-((5-methylfuran-2-yl) methyl)quinazolin-4-amine 5d

White solid, Yield: 57%, ^{1}H NMR (500 MHz, DMSO-d_6) δ 8.86 (t, *J* = 5.7 Hz, 1H), 8.60 (d, *J* = 2.1 Hz, 1H), 8.50 (s, 1H), 8.13 (dd, *J* = 8.7, 2.0 Hz, 1H), 7.75 (d, *J* = 8.7 Hz, 1H), 6.98 (d, *J* = 2.3 Hz, 2H), 6.57 (d, *J* = 2.3 Hz, 1H), 6.22 (d, *J* = 3.1 Hz, 1H), 6.00 (d, *J* = 3.0 Hz, 1H), 4.74 (d, *J* = 5.5 Hz, 2H), 3.84 (s, 6H), 2.23 (s, 3H). ^{13}C NMR (126 MHz, DMSO-d_6) δ 160.84, 159.13, 154.89, 150.56, 150.12, 148.59, 140.94, 137.00, 131.22, 127.84, 120.24, 114.88, 108.02, 106.31, 105.18, 99.11, 55.23, 36.98, 13.16. (ESI-MS): *m/z* 376.07 $[M+H]^+$.

Synthesis of 7-(3,4-dimethoxyphenyl)-*N*-((5-methylfuran-2-yl) methyl)quinazolin-4-amine 5e

White solid, Yield: 61%, ^{1}H NMR (500 MHz, DMSO-d_6) δ 8.80 (t, *J* = 5.7 Hz, 1H), 8.55 (d, *J* = 2.1 Hz, 1H), 8.48 (s, 1H), 8.11 (dd, *J* = 8.7, 2.0 Hz, 1H), 7.74 (d, *J* = 8.7 Hz, 1H), 7.38 (d, *J* = 7.0 Hz, 2H), 7.11 – 7.06 (m, 1H), 6.21 (d, *J* = 3.1 Hz, 1H), 5.99 (dd, *J* = 3.1, 1.3 Hz, 1H), 4.75 (d, *J* = 5.5 Hz, 2H), 3.89 (s, 3H), 3.81 (s, 3H), 2.23 (s, 3H). ^{13}C NMR (126 MHz, DMSO-d_6) δ 159.02, 154.52, 150.18, 148.72, 148.04, 137.21, 131.64, 131.04, 127.80, 119.28, 119.24, 114.97, 112.02, 110.64, 107.99, 106.30, 55.64, 55.45, 36.97, 13.15. (ESI-MS): *m/z* 376.03 $[M+H]^+$.

2.1.6. X-ray diffraction analysis

The molecular and crystal structure of compound 3h was determined through single-crystal X-ray diffraction. Data were collected on a Bruker APEX II QUAZAR three-circle diffractometer. The structure was solved with the SHELXT 2014/5 structure solution program [15]. via Intrinsic Phasing and refined by Least Squares minimization using the SHELXL-2018/3 software [16], all within the Olex2 1.3(26) platform [17]. The crystallographic information files (CIFs) can be accessed from the CSD database at https://www.ccdc.cam.ac.uk/structures/ (CCDC numbers: 2475869). Additional details on crystal data and structure refinement can be found in Table SM1.

2.2. In Vitro analysis

2.2.1. Cell Culture

The C2C12 cell line (CRL-1772) was purchased from the American Type Culture Collection (ATCC, Manassas, VA, USA). Cells were cultured in high-glucose Dulbecco's Modified Eagle's Medium (DMEM; Gibco, Thermo Fisher Scientific, Waltham, MA, USA) supplemented with 10% fetal bovine serum (FBS; Gibco, Thermo Fisher Scientific) and 1% penicillin–streptomycin (Gibco, Thermo Fisher Scientific). The cells were maintained at 37°C in a humidified incubator with 5% CO_2 and propagated in 75 cm^2 culture flasks.

2.2.2. Cell proliferation assay

Cell viability and proliferation were determined using the MTT assay (SERVA Electrophoresis GmbH, Heidelberg, Germany). Briefly, C2C12 cells were plated in 96-well plates at a density of 7×10^4 cells per well and allowed to adhere for 24 h. The cells were then exposed to the test compound at a final concentration of 10 μM for 48 h under standard

incubation conditions (37°C, 5% CO_2). Untreated cells cultured in complete medium served as the control group. Following treatment, 10 μL of MTT solution (5 mg/mL in PBS) was added to each well, and the plates were incubated for an additional 2 h at 37°C. The culture medium was carefully removed, and 100 μL of dimethyl sulfoxide (DMSO; AppliChem GmbH, Darmstadt, Germany) was added to each well to solubilize the resulting formazan crystals. After gentle agitation for 30 min, absorbance was recorded at 570 nm using a microplate reader (Agilent Technologies, Winooski, VT, USA). Proliferation rates were calculated and presented as percentages relative to the control group.

2.2.3. Statistical Analysis

Results were reported as mean ± standard deviation (SD). Statistical evaluation was conducted using GraphPad Prism version 10.3.1 (GraphPad Software, San Diego, CA, USA). Comparisons between treated and control groups were performed using Student's t-test, with $p < 0.05$ considered statistically significant.

2.3. In silico studies

2.3.1. Molecular docking

The molecular docking studies were performed using the AlphaFold structure of the P08574 (CY1_HUMAN) protein in Schrödinger Maestro [18]. Protein structures were refined using the Protein Preparation Wizard, adjusting protonation states and optimizing geometry with the OPLS4 force field [19]. Binding sites were predicted using the Schrödinger Binding Site Identification module. The top-scored binding site was selected for grid generation. A receptor grid was generated with the grid box centred at coordinates (−10.0, −2.0, 6.0) representing the predicted binding region. The outer grid box dimensions were defined as 46 × 46 × 46 Å, while the inner grid box dimensions were set to 10 × 10 × 10 Å, confirming sufficient coverage of the binding region. The receptor grid was saved as a .maegz file and used for the docking calculations. Compound structures were prepared in ChemDraw, converted to 3D using LigPrep, minimized with OPLS4, and processed for relevant tautomers and ionization states at physiological pH. Docking was carried out in Glide using standard precision (SP) mode with flexible ligands, and results were evaluated using the Glide docking score [20].

2.3.2. Quantum chemical simulations

All density functional theory (DFT) calculations were done using Gaussian 09 in combination with the Gauss View 6.0 software package [21,22]. Geometry optimizations were performed at the B3LYP/6-31G (d, p) level to determine the electronic properties, including frontier molecular orbitals and global reactivity descriptors. Analytical vibrational frequency calculations were subsequently performed at the same level of theory to verify the nature of the optimized structure. The absence of imaginary frequencies confirmed that the optimized geometry corresponds to a true minimum on the potential energy surface.

Interaction energies for the compound were calculated using the supermolecule approach and improved for basis set superposition error (BSSE) by the counterpoise method [23]. The analysis is based on the wavefunction, including the quantum theory of atoms in molecules (QTAIM) [24], noncovalent interaction (NCI), electron localization function (ELF) [25], reduced density gradient (RDG) analysis, and electrostatic potential (ESP) calculations, were performed using the Multiwfn 3.8 program [26] based on the converged DFT wavefunctions. Visualization of NCI isosurfaces was carried out using VMD 1.9.3 [27].

Molecular electrostatic potential (MEP) surfaces were produced using GaussView 6.0 at an isodensity value of 0.001 a.u. Global chemical reactivity descriptors were calculated within the framework of conceptual density functional theory using the energies of the frontier molecular orbitals [28,29].

3. Result and discussion

3.1. Chemistry

The synthesized compounds (**3a-3h** and **5a-5e**), summarized in Table 1, were obtained through a series of selective reactions as outlined in Scheme 1.

Initially, 4,7-dichloroquinazoline was reacted with various boronic acid derivatives under standard Suzuki–Miyaura coupling conditions to afford mono-substituted products (**3a** to **3c**). In a separate series, the 4,7-dichloroquinazoline was treated with (5-methylfuran-2-yl)methanamine to produce the monosubstituted **5a**. In this series, also when an excess of (5-methylfuran-2-yl) methanamine was used, bis-substituted compound **5b** was generated. Finally, previously synthesized monosubstituted compounds were further functionalized via additional Suzuki coupling with a variety of boronic acids, resulting in bis-substituted products (**3d**-**3h**), (**5c**-**5e**) featuring diverse substitution patterns. All compounds were synthesized in moderate to good yields. Their structures were confirmed and characterized by various spectroscopic techniques, including ^1H and ^{13}C NMR spectroscopy, mass spectrometry (ESI-MS), and, where applicable, Single-crystal X-ray crystallography.

The ^1H NMR spectra of all compounds displayed a characteristic singlet in the range of 8.51–9.45 ppm, corresponding to the proton at the 2-position of the quinazoline moiety. In addition, compounds **5c**–**5e** exhibited a triplet and a doublet in the ranges of 8.45–8.86 ppm and 4.38–4.75 ppm, respectively, attributed to the –NH proton of the secondary amine and the $–CH_2$ protons. The ^{13}C NMR spectra also featured a distinct signal for the carbon at the 2-position of the quinazoline ring, observed between 158.85 and 168.13 ppm. In particular, the ^1H NMR spectrum of compound **3g** exhibited a singlet at 3.86 ppm, corresponding to the protons of the dimethoxy groups. The protons of the phenyl group at the 7-position of the quinazoline moiety appeared as a doublet and a triplet at 7.02 ppm and 6.64 ppm, respectively. The remaining aromatic protons were observed in the range of 6.77–8.15 ppm. The ^{13}C NMR spectrum of compound **3g** showed a characteristic signal for the dimethoxy carbons at 55.91 ppm, while the aromatic carbon resonances appeared between 101.29 and 161.55 ppm. The carbon at the 2-position of the quinazoline moiety exhibited a distinct signal at 166.41 ppm. The ESI-MS spectrum showed a molecular ion peak at *m/z* 410.99, corresponding to $[M + H]^+$ for the molecular formula $C_{23}H_{17}F_3N_2O_2$ (calculated *m/z* 411.13). In another example, the ^1H NMR spectrum of compound **5d** exhibited a singlet at 2.23 ppm, characteristic of the methyl protons. The proton of the secondary amine (–NH) appears as a triplet at 8.86 ppm, while the CH_2 protons appear as a triplet at 4.74 ppm. The protons of the phenyl ring at the 7-position of the quinazoline moiety appeared as a doublet and a triplet at 6.97 ppm and 6.57 ppm, respectively, while the protons of the dimethoxy groups were observed as a singlet at 3.84 ppm. Additionally, the protons at the 3- and 4-positions of the furan moiety appeared as doublets at 5.99 and 6.21 ppm, respectively. The remaining aromatic protons were observed in the range of 7.74–8.60 ppm. The ^{13}C NMR spectrum of **5d** exhibited a characteristic signal for the methyl carbon at 13.16 ppm, and the methylene ($–CH_2$) carbon appeared at 36.98 ppm. The dimethoxy carbons were observed at 55.23 ppm. Additionally, a distinct signal for the carbon at the 2-position of the quinazoline moiety was detected at 160.84 ppm, while the aromatic carbon resonances appeared in the range of 106.95 to 159.81 ppm. The ESI-MS spectrum showed a molecular ion peak at *m/z* 376.07, corresponding to $[M + H]^+$ for the molecular formula $C_{22}H_{21}N_3O_3$ (calculated *m/z* 376.16).

3.2. X-ray crystallography analysis

The structural properties of compound 3h were analysed using X-ray crystallography. Data summary of crystallographic parameters is given in Table SM1. The atomic numbering and 50% probability displacement

Table 1
Structures, substituents, and cell proliferation activities of the synthesized quinazoline derivatives (3a–3h and 5a–5e).

Entry	R_1	R_2	Cell Proliferation (%) (10μM)
Control	-	-	100
ML-167	Drug repurposing	-	60
Metformin	**Reference**	-	93
3a	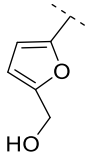	-	97
3b	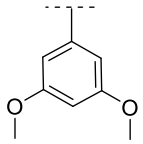	-	64
3c	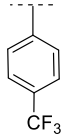	-	91
3d	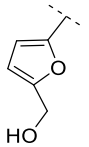	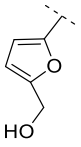	85
3e	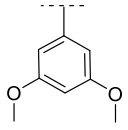	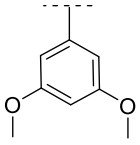	63
3f	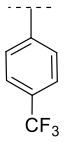	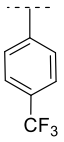	96
3g	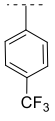	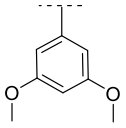	74
3h	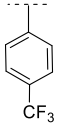	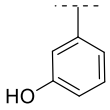	82
5a	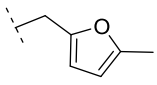	-	96
5b	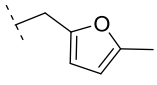	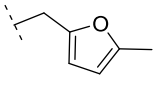	86

Table 1 (*continued*)

Entry	R_1	R_2	Cell Proliferation (%) (10μM)
5c	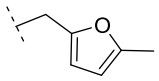	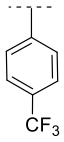	93
5d	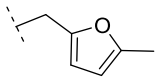	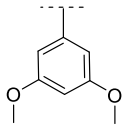	55
5e	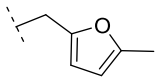	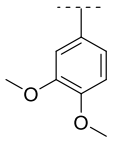	53

ellipsoid of the complexes are shown in Fig. 2.

Compound 3h crystallizes in the triclinic crystal system with the P-1 space group. The asymmetric unit contains two independent molecules (A and B). The dihedral angles between the quinazoline core and the methoxy- and trifluoromethyl-substituted phenyl rings are 32.55° and 66.77° for molecule A, and 31.47° and 65.82° for molecule B, respectively, indicating a non-coplanar molecular conformation. The dihedral angles between the two aromatic rings are 63.40° for molecule A and 56.43° for molecule B, reflecting a twisted geometry that may influence molecular packing. The relatively large anisotropic displacement observed for the fluorine atoms of the terminal CF_3 group may be attributed to the inherent rotational/torsional flexibility of the CF_3 moiety around the C–CF_3 bond. Such rotational motion is commonly observed for CF_3 substituents and can result in elongated thermal ellipsoids. The two independent molecules form a dimer through C37–H37···O1 and C21–H21···O2 interactions Fig. 3. These dimers extend along the *b* axis through O1–H1···N1^{i} and O2–H2···N4^{i} interactions (symmetry code: (*i*) x, -1+y, z), forming a one-dimensional chain in the crystal structure Fig. 4. Additionally, two non-classical C–H···C hydrogen bonding interactions C42–H42···C2 ^{ii} and C41–H41···C17 ^{iii}, with H···C distances of 2.88 Å and 2.83 Å, respectively, connect these chains along the a-axis (symmetry code: (*ii*) -1+x, y, z, (*iii*) -1+x, -1+y, z). As a result, a two-dimensional supramolecular layer is formed in the *ab* plane, stabilized by both classical and weak hydrogen bonding interactions (Fig. 5). The complete crystallographic data have been deposited with the Cambridge Crystallographic Data Centre (No. 2475869).

3.3. Geometric analysis

The molecular structure was further validated by comparing the experimental X-ray data with the optimized geometry of compound 3h obtained at the B3LYP/6-31G(d,p) level. Selected bond angles and bond lengths are presented in Table 2. The calculated geometrical parameters well align with the experimental values. The mean absolute deviations are 2.2° for bond angles and 0.028 Å for bond lengths (excluding hydrogen atoms), indicating that the applied theoretical level is reliable enough to reproduce the molecular structure. The C–C bond distances of the aromatic ring (1.368–1.416 Å) are consistent with an extensively delocalized π-electron system. The optimized structure keeps the bond length calculated values ranging from 1.392 to 1.407 Å. The associated internal ring angles (117–125°) further support the conjugation within the aromatic framework. The slight distortions in angles observed at substituted carbon atoms show steric and electronic effects imposed by

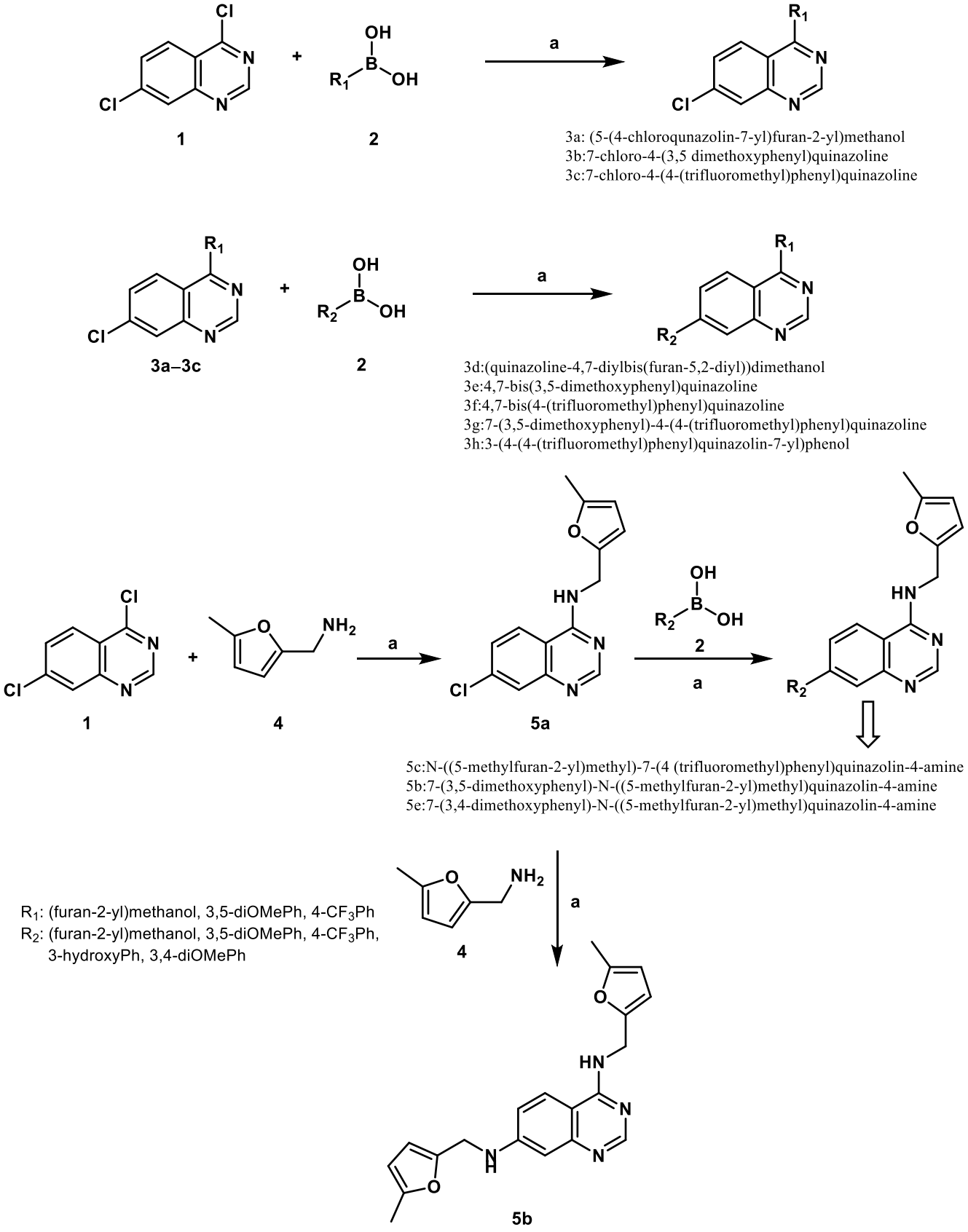

Scheme 1. Synthesis of ML-167 derivatives **(3a-3h)** and **(5a-5e)**. Reagents and conditions: a) Cs_2CO_3, $Pd(dppf)Cl_2$, THF, 160°C, MW.

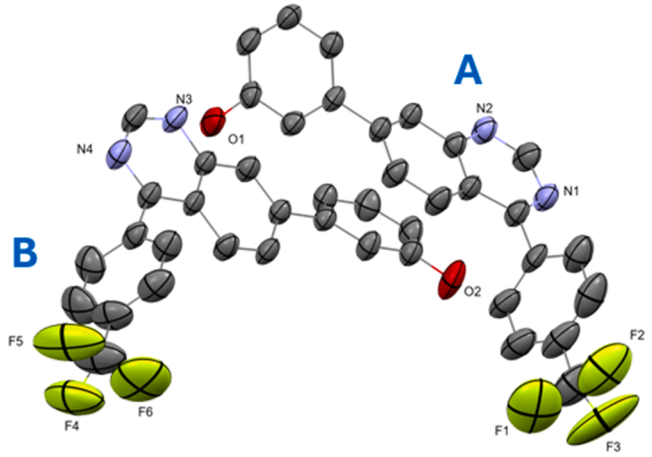

Fig. 2. Molecular structure of compound 3h showing 50% probability displacement ellipsoids. Hydrogen atoms have been omitted for clarity.

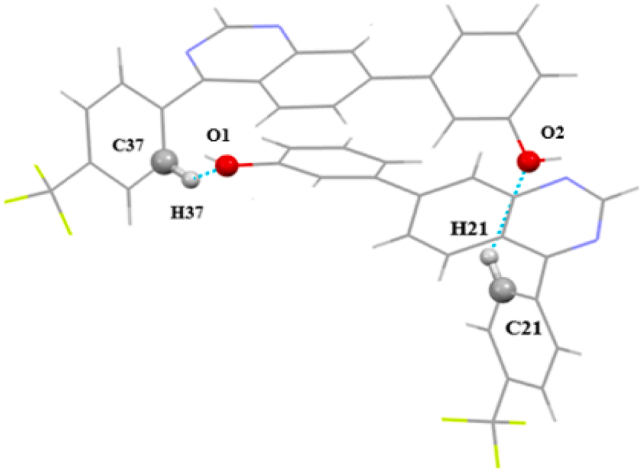

Fig. 3. Dimer formation in the asymmetric unit via intermolecular C37–H37···O1 and C21–H21···O2 hydrogen-bonding interactions.

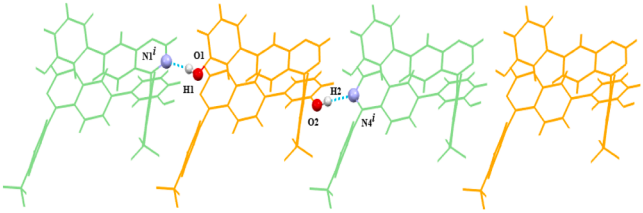

Fig. 4. One-dimensional chain formed by extension of the dimers along the *b* axis through intermolecular O1–H1···$N1^{i}$ and O2–H2···$N4^{i}$ hydrogen bonds [symmetry code: (*i*) x, −1 + y, z].

the CF_3 substituent and adjacent heteroatoms. The C–N bond lengths (1.304–1.372 Å) lie between single and double bond values, showing partial double-bond character due to π-conjugation within the heterocyclic ring. This explanation is supported by the extended N–C–N bond angles (e.g., 129.1(3)°and 128.6(3)°), which considerably surpass the ideal 120° value expected for sp^2 hybridization. The hydroxyl groups exhibit nearly ideal tetrahedral C–O–H bond angles (~110° calculated; ~109.5° experimentally). A more pronounced deviation is observed for the O–H bond length (0.820 Å vs. 0.99 Å), which arises from the inherent limitations of X-ray diffraction in determining hydrogen atom positions accurately. The -CF_3 group adopts tetrahedral geometries with

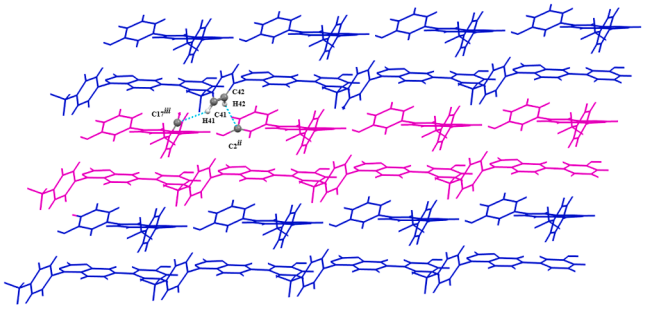

Fig. 5. Crystal packing showing the linkage of one-dimensional chains along the *a* axis through non-classical C–H···C interactions, namely C42–H42···$C2^{ii}$ and C41–H41···$C17^{iii}$, with H···C distances of 2.88 and 2.83 Å, respectively [symmetry codes: (*ii*) −1 + x, y, z; (*iii*) −1 + x, −1 + y, z].

slight distortion in both theoretical (104.0–111.4°) and experimental structures (104.0–111.4°). Small differences between the two structures can be attributed to intermolecular interactions, the strong electron-withdrawing character of fluorine atoms, and crystal packing effects present in the solid state but absent in the gas-phase calculations.

3.4. *In vitro study*

The impact of the synthesized compounds on C2C12 cell proliferation was assessed after 48 h exposure to each compound (10 μM), using the MTT assay. The in vitro proliferation percentages of the tested ML-167 derivatives are summarized in Table 1. Overall, ML-167 derivatives resulted in variable cellular responses under the experimental conditions (Fig. 6).

The reference compound ML-167 showed a significant reduction in cell viability, while metformin exerted only a limited effect on proliferation. Among the evaluated derivatives, several compounds maintained cell viability at levels comparable to the untreated control group, indicating good cellular response at the tested concentration. This observation suggests that these compounds do not negatively affect C2C12 myoblast viability under the experimental conditions. Compounds 3a, 3f, 5a, and 5c preserved proliferation levels close to those of the control group. In contrast, a subset of derivatives was associated with a reduction in cell proliferation, with compounds 5d and 5e showing the most pronounced effects, followed by 3b and 3e. Overall, these findings indicate that ML-167 derivatives exert compound-dependent effects on C2C12 myoblast viability, with several derivatives demonstrating a capacity to maintain cellular proliferation. Such properties may be of interest in the context of preserving muscle cell viability relevant to sarcopenia-related conditions.

3.5. *In silico studies*

3.5.1. *DFT Calculations on Chemical Reactivity*

The optimized molecular geometry of compound 3h obtained at the B3LYP/6-31G(d,p) level of theory is shown in Fig. 7. The optimized structure served as the starting geometry for all subsequent quantum chemical analyses, including frontier molecular orbital (HOMO–LUMO), molecular electrostatic potential (MEP), and non-covalent interaction analysis.

The electronic structure and reactivity of the molecule were analysed in terms of its frontier molecular orbitals (FMOs), which provide insight into delocalized molecular orbital densities. The spatial arrangement of the HOMO and LUMO orbitals is shown in Fig. 8. The HOMO is particularly positioned across the quinazoline core and the nearby aromatic ring, with partial contribution from the methoxy-substituted phenyl moiety, displaying that these regions correspond to the prime electron-donating sites. In contrast, the LUMO is mostly assigned over the quinazoline frame and the trifluoromethyl-substituted phenyl ring,

Table 2
Selected experimental (X-ray) and calculated (DFT/B3LYP) bond lengths (Å) and angles (°) for molecules A and B in compound 3h.

No.	Angle	X-ray (°)	B3LYP (°)	Bond	X-ray (Å)	B3LYP (Å)
Molecule A						
1	N1A–C13A–N2A	129.1(3)	126.09	C13A–N2A	1.304(5)	1.318
2	C13A–N1A–C14A	115.6(3)	118.35	C14A–N1A	1.319(4)	1.323
3	C9A–N2A–C13A	115.6(3)	116.67	C13A–N1A	1.356(4)	1.368
4	C7A–C8A–C9A	121.4(3)	119.72	C9A–N2A	1.372(3)	1.370
5	C11A–C12A–C14A	124.3(3)	120.99	C2A–O1A	1.361(4)	1.386
6	C12A–C14A–N1A	121.8(3)	121.07	C6A–C7A	1.482(4)	1.487
7	C2A–O1A–H1A	109.5	110.10	C14A–C15A	1.486(5)	1.485
8	C18A–C19A–F1A	112.3(5)	111.10	C–F (CF_3 group A)	1.303–1.316	1.376–1.378
9	C18A–C19A–F2A	112.5(5)	111.07	Aromatic C–C (range)	1.368–1.422	1.393–1.407
10	C18A–C19A–F3A	111.4(5)	112.50	—	—	—
11	F1A–C19A–F2A	104.9(5)	108.73	—	—	—
12	F1A–C19A–F3A	111.3(5)	106.64	—	—	—
13	F2A–C19A–F3A	104.0(5)	106.56	—	—	—
Molecule B						
14	N3B–C34B–N4B	128.6(3)	126.51	C23B–O2B	1.361(4)	1.386
15	C32B–N3B–C34B	115.7(3)	118.07	—	—	—
16	C34B–N4B–C35B	115.7(3)	116.54	—	—	—
17	C23B–O2B–H2B	109.5	110.15	—	—	—
18	C22B–C23B–O2B	117.1(3)	116.77	—	—	—
19	C24B–C23B–O2B	123.1(3)	123.58	—	—	—
20	C39B–C40B–F4B	113.7(5)	110.63	—	—	—
21	F4B–C40B–F5B	104.0(5)	107.51	—	—	—
22	C30B–C33B–C35B	125.0(3)	125.58	—	—	—

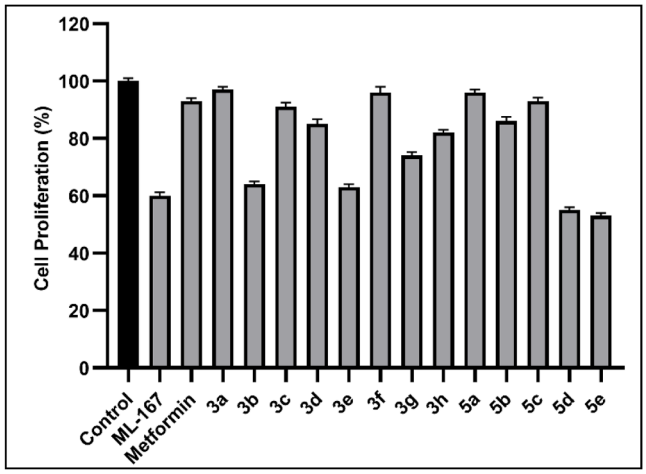

Fig. 6. Effects of ML-167 derivatives (10 μM, 48 h) on C2C12 cell viability determined by MTT assay. ML-167 and metformin were used as reference compounds. Data represent mean ± SD (n ≥ 3).

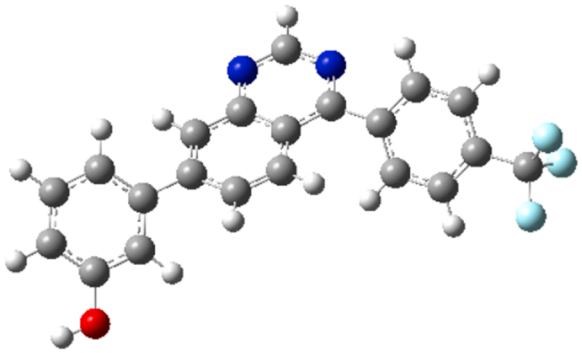

Fig. 7. DFT-optimized molecular geometry of compound 3h calculated at the B3LYP/6-31G(d,p) level of theory in the gas phase.

demonstrating a favourable electron-accepting region. The partition of HOMO-LUMO frontier orbitals indicates an intramolecular charge

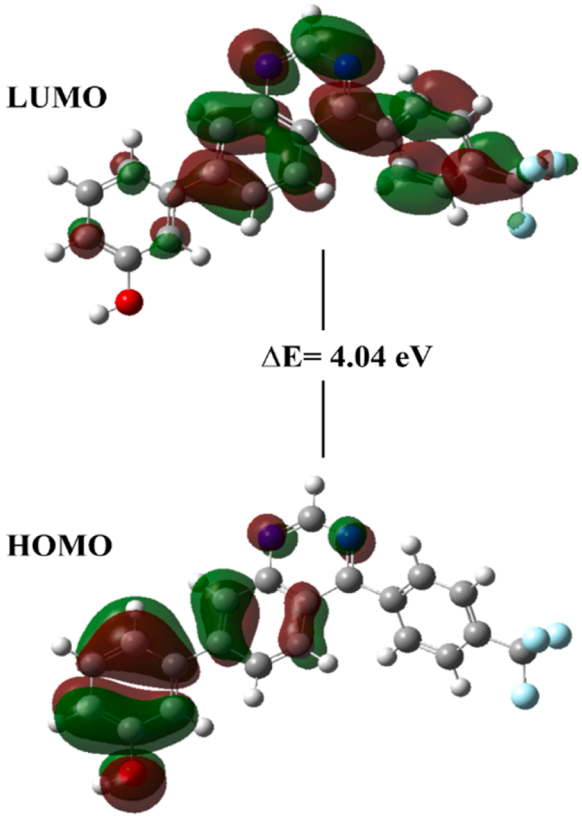

Fig. 8. HOMO-LUMO surface map of **3h**.

transfer movement from the electron-rich system to the electron-deficient CF_3-substituted ring via the conjugated quinazoline framework. The computed HOMO and LUMO energies of -6.77 eV and -2.73 eV, respectively, result in a HOMO–LUMO energy gap (ΔE) of 4.04 eV, revealing a sensible balance between controlled chemical reactivity and stability. This gap indicates adequate kinetic stability while allowing the molecule to participate in intermolecular interactions, consistent with the global reactivity descriptors.

These electronic features identified in the FMO analysis are further supported by the molecular electrostatic potential (ESP) surface (Fig. 9), which shows electron-rich regions around heteroatoms and electron-deficient regions near the aromatic rings. This charge distribution explains the observed intermolecular C–H···O/N and C–H···F interactions in the crystal structure. Additionally, global reactivity descriptors such as chemical potential (μ), electronegativity (χ), global hardness (η), softness (S), and electrophilicity index (ω)were calculated using Koopmans' theorem within the framework of conceptual DFT. The calculated HOMO–LUMO energy gap (ΔE = 4.04 eV) and global hardness (η = 2.02 eV) indicate moderate resistance toward charge transfer and good kinetic stability. The electronegativity value (χ = 4.75 eV) displays a substantial tendency to attract electrons, supporting the presence of electron-withdrawing substituents in the molecular framework.

The low softness value (S = 0.247 eV^{-1}) indicates controlled chemical reactivity and low polarizability. Moreover, the electrophilicity index (ω = 5.59 eV) indicates a pronounced electron-accepting capability, consistent with the charge-transfer character observed in the HOMO–LUMO analysis.

3.6. Topological analysis of noncovalent interactions

3.6.1. Noncovalent Interaction (NCI) and Reduced Density Gradient (RDG) Analysis

Noncovalent interaction (NCI) analysis, combined with the reduced density gradient (RDG) method, was performed to visualize the weak intermolecular interactions governing the crystal packing of compound **3h** (Fig. 10). The RDG versus *sign(λ₂)ρ* plot exhibits low-density spikes close to zero values, indicating the presence of weak noncovalent interactions (Fig. 11). These results provide detailed insight into the nature of the intermolecular interactions present within the crystal structure.

The resulting three-dimensional NCI isosurfaces are predominantly green, highlighting the dominance of weak dispersive (van der Waals) interactions. These green regions are primarily located between neighbouring aromatic rings and along C–H···F and C–H···O contacts, consistent with the intermolecular interactions identified by single-crystal X-ray diffraction. The blue isosurfaces are located in regions corresponding to the O–H···N contacts, indicating strong attractive interactions consistent with classical hydrogen bonding within the crystal packing. The relatively limited extent of the blue regions suggests that hydrogen bonding contributes less to the overall crystal stabilization than the dispersive interactions. Small red isosurfaces, confined to intramolecular regions, correspond to steric repulsion.

In general, the NCI-RDG analysis indicates that the crystal structure

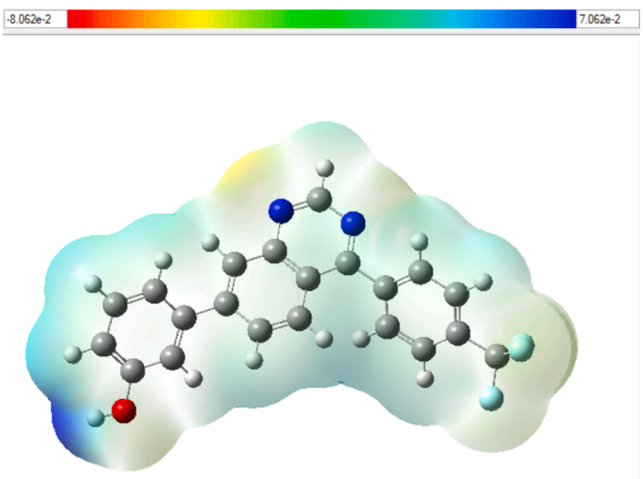

Fig. 9. MEP surface map of **3h**.

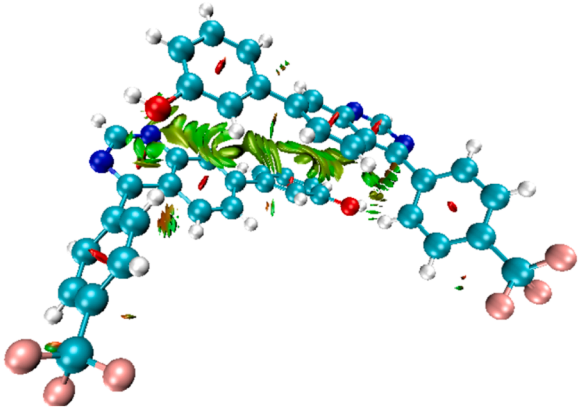

Fig. 10. Three-dimensional noncovalent interaction (NCI) isosurface map of compound **3h** illustrating the spatial distribution of weak intermolecular interactions. Blue, green, and red isosurfaces correspond to attractive interactions, weak dispersive (van der Waals) interactions, and steric repulsion, respectively.

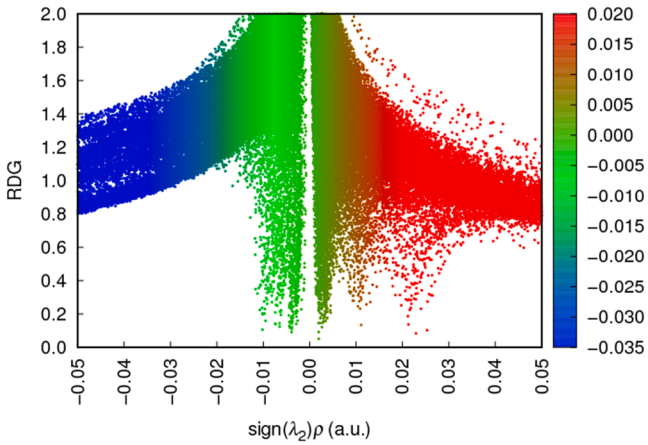

Fig. 11. Reduced density gradient (RDG) scatter plot of compound 3h as a function of sign(λ₂)ρ. The color scale distinguishes attractive interactions (blue), weak dispersive (van der Waals) interactions (green), and steric repulsion (red).

is stabilized primarily by weak noncovalent interactions, including van der Waals interactions, C–H···O, C–H···F, and π-related interactions. These interactions contribute to the organization and stabilization of the supramolecular chains and layers within the crystal, in agreement with the experimental X-ray diffraction results and further supported by the ELF and QTAIM analyses.

3.6.2. Electron localization function (ELF) analysis

The electron localization function (ELF) map of compound 3h is shown in Fig. 12. It provides detailed insight into the bonding characteristics and electron localization within the molecule. High ELF values are localized around the nitrogen and oxygen atoms, reflecting the localization of lone-pair electrons and their role as hydrogen-bond acceptors. In contrast, relatively low ELF values are observed over the aromatic rings, indicating electron delocalization throughout the conjugated phenyl substituents and quinazoline framework, consistent with the conjugated molecular structure.

Interestingly, no ELF basins are observed in the regions corresponding to the intermolecular C–H···O and C–H···F contacts, consistent with the closed-shell, noncovalent nature of these interactions. These findings support the presence of weak intermolecular interactions inferred from the crystallographic analysis. Furthermore, the delocalized π-electron distribution facilitates intramolecular charge transfer,

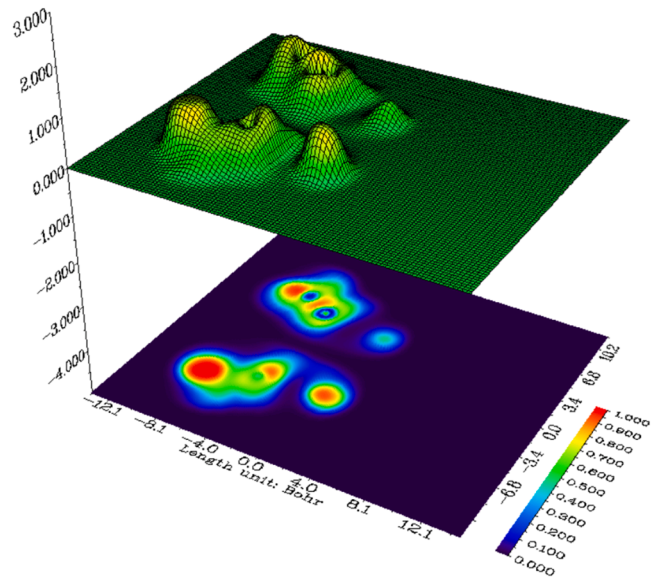

Fig. 12. Electron localization function (ELF) shaded surface map of compound 3h together with its two-dimensional projection, illustrating the distribution of localized electron density associated with chemical bonds and lone-pair electrons, as well as electron delocalization over the conjugated molecular framework.

in agreement with the HOMO–LUMO analysis.

3.6.3. *Quantum Theory of Atoms in Molecules (QTAIM) Analysis*

A Quantum Theory of Atoms in Molecules (QTAIM) analysis was performed to characterize the nature of the weak intermolecular interactions. The molecular graph obtained from the QTAIM analysis is shown in Fig. 13. The topological parameters evaluated at the bond critical point (BCP) include the electron density (ρ), the Laplacian of the electron density ($\nabla^2\rho$), the kinetic energy density G(r), the potential energy density V(r), the total energy density H(r), and the G(r)/|V(r)| ratio. The electron density at the bond critical point of the F74···H21 interaction is ρ = 0.01396 a.u., which falls within the range typically reported for weak hydrogen bonds and other noncovalent interactions. The positive Laplacian of the electron density ($\nabla^2\rho$ = 0.0806 a.u.) indicates depletion of electron density in the bonding region, confirming the closed-shell nature of this interaction. The positive kinetic energy density (G(r) = 0.01639 a.u.) together with the negative potential energy density (V(r) = –0.01264 a.u.) are consistent with the predominantly closed-shell character of this interaction rather than shared-electron (covalent) character. In addition, the positive total energy density (H(r) = +0.0038 a.u.) at the bond critical point is characteristic of weak, noncovalent interactions. Furthermore, the calculated G(r)/|V(r)| ratio of 1.30 confirms the purely closed-shell character of the interaction. These results demonstrate that the F74···H21 interaction is predominantly noncovalent in nature and is stabilized mainly by dispersive and electrostatic contributions. Overall, the QTAIM results

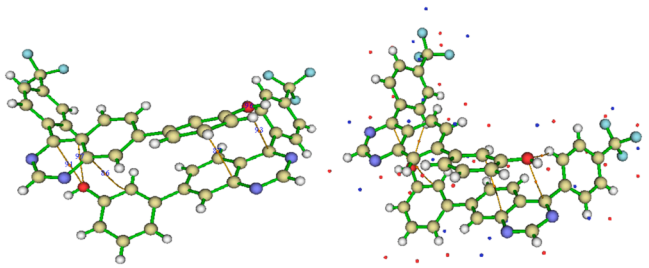

Fig. 13. Molecular structure using Multiwfn with critical points.

are in good agreement with the ESP and NCI analyses, supporting the important role of weak C–H···F interactions in stabilizing the supramolecular architecture observed in the crystal structure.

From the crystal structure, the two molecules forming the dimer are linked through two C–H···O contacts (C37–H37···O1 and C21–H21···O2) with H···O distances of 2.693 and 2.641 Å, respectively. To quantitatively evaluate these intermolecular interactions, the interaction energy of the crystallographic dimer was calculated using the counterpoise-corrected supermolecule approach. The raw interaction energy was −5.21 kcal mol^{-1}, whereas the BSSE-corrected value was +0.81 kcal mol^{-1} at the B3LYP/6-31G(d,p) level of theory. The small, corrected interaction energy suggests that these pairwise contacts alone provide only limited stabilization of the isolated dimer, indicating that the observed dimeric arrangement is primarily reinforced by cooperative crystal-packing effects. These findings complement the NCI, RDG, ELF, and QTAIM analyses by providing a quantitative assessment of the weak intermolecular interactions.

3.7. *Structure–Activity Relationship (SAR) and Molecular Modeling Studies*

The synthesized compounds are the derivatives of the quinazoline scaffold, with different substituents at the 4- and 7-positions, including chloro, methoxyphenyl, aryl, aminomethyl-furan, and trifluoromethylphenyl moieties. This structural framework features a planar heteroaromatic core that enables π–π stacking interactions with the predicted binding cavity. At the same time, the chloro, amino, and aryl substituents are capable of forming hydrogen bonds and hydrophobic interactions that could support receptor engagement. As these derivatives were designed as modulators for sarcopenia-related pathways, improvement of cell proliferation was considered an indication of biological activation. The predicted docking interaction details (**Table SM2**) and docking diagrams (**Figure SM 1d**) are given in the supplementary file.

Compound **5a** showed the highest cell proliferation rate (96%) at 10 μM among the mono-substituted quinazoline-4-amine series. It showed a favorable interaction profile with a moderate docking score, characterized by hydrophobic contacts with Phe114, Lys118, and Asp128, as well as halogen-bond interactions with Cys124 and Ser126. The presence of a 4-amino group, combined with a connected 7-chloro substituent, stabilizes conformational flexibility and electronic distribution.

Within the bis-substituted series, compound **5b** presented a slightly lower proliferation rate (86%) with a favorable docking score and established strong salt bridge interactions with Asp128 and Asp196. Regardless of its promising docking score, the compound showed limited proliferation response, suggesting that binding affinity alone does not determine biological activity.

The quinazoline derivatives with diaryl and large aromatic ring substitution, such as compounds **3a** and **3f,** showed comparatively strong docking scores with a proliferation rate of ~96–97%. These compounds mediated multiple hydrophobic interactions within the binding cavity. In the case of compound **3a**, there are additional H-bond interactions observed with Ser126, Pro194, and Asp196. However, the presence of sterically bulky groups limited the flexibility.

Compound **3e** and its related derivatives **5d** and **5e**, holding electron-donating methoxy substituents, explain the low proliferative effects of 63%, 55%, and 53%, respectively. Although these compounds exhibited multiple hydrophobic and hydrogen-bond interactions with the binding site, the excessive effect of electron-donating groups and expanded aromatic volume may adversely affect the activation potential. Similarly, in the case of trifluoromethyl-containing derivatives with moderate docking scores, they show lower proliferation rates, indicating that strong electron-withdrawing effects might be insufficient to strengthen biological activity.

Overall, the docking results were in good agreement with the biological evaluation. Compounds demonstrating balanced hydrophilic and

hydrophobic interactions, particularly compounds 3a, 3f, and 5a, mostly showed higher C2C12 proliferation. On the contrary, compounds with excessive steric/electronic effects and less favourable interaction profiles displayed reduced biological activity, supporting the proposed structure–activity relationship.

4. Conclusion

In conclusion, this study successfully designed, synthesized, and characterized a series of novel quinazoline-based ML-167 derivatives as potential CYC1-targeting agents for the therapy of sarcopenia. The synthesized derivatives of ML-167 were structurally characterized and evaluated using a multidisciplinary approach that combined synthetic chemistry, crystallographic analysis, computational studies, and biological assessment. The in vitro evaluation in C2C12 cells demonstrated that compounds 3a, 3f, and 5a exhibited the most promising effects on cell proliferation, identifying these derivatives as potential lead structures within the investigated quinazoline series. Molecular docking demonstrated favourable binding profiles of the synthesized derivatives within the CYC1 cavity, primarily supported by dispersive and hydrophobic contacts, with a few hydrogen-bond interactions. DFT, FMO, RDG-NCI, and QTAIM analyses further explained the electronic suitability of the analogues, emphasizing charge distribution patterns consistent with their observed binding patterns. The integration of the in vitro biological results with the crystallographic and computational findings highlights a structure–activity correlation within the quinazoline scaffold and provides a rational basis for understanding the differences in activity among the investigated derivatives. Although further mechanistic and in vivo validation studies are required, the present findings provide a rational foundation for developing quinazoline-based modulators as potential therapeutic candidates for muscle-related disorders.

Funding

Molius and Trustlife Therapeutics financially supported this study.

CRediT authorship contribution statement

Sajda Ashraf: Writing – review & editing, Writing – original draft, Visualization, Validation, Methodology, Investigation, Formal analysis, Data curation, Conceptualization. **Shabnam Alizadeh:** Writing – review & editing, Writing – original draft, Methodology, Investigation, Formal analysis, Data curation. **Issam Ameziane El Hassani:** Methodology, Formal analysis, Data curation. **Aybuke Ozturk:** Formal analysis, Data curation. **Naime Ceren Suer:** Formal analysis, Data curation. **Woonghee Kim:** Validation, Formal analysis, Data curation. **Gonca Candan:** Writing – review & editing, Writing – original draft, Validation, Formal analysis, Data curation. **Gizem Batı Ayaz:** Writing – review & editing, Writing – original draft, Validation, Methodology, Formal analysis, Data curation. **Murat Ozdemir:** Supervision, Formal analysis, Data curation. **Güldeniz Yeşilyurt:** Formal analysis, Data curation. **Essam Hanashalshahaby:** Supervision, Formal analysis. **Hasan Turkez:** Project administration. **Adil Mardinoglu:** Resources, Project administration, Funding acquisition.

Declaration of competing interest

The authors declare the following potential competing financial interests: A patent application covering the novel ML-167 analogues and their therapeutic uses described in this manuscript, entitled "Novel compounds and their pharmaceutical uses", has been filed and is currently under review. The remaining authors declare no competing financial interests.

Supplementary materials

Supplementary material associated with this article can be found, in the online version, at doi:10.1016/j.molstruc.2026.147455.

Data availability

Data will be made available on request.

References

[1] A.J. Cruz-Jentoft, A.A. Sayer, Sarcopenia, The Lancet 393 (2019) 2636–2646, https://doi.org/10.1016/S0140-6736(19)31138-9.
[2] S. Yuan, S.C. Larsson, Epidemiology of sarcopenia: Prevalence, risk factors, and consequences, Metabolism 144 (2023) 155533, https://doi.org/10.1016/j.metabol.2023.155533.
[3] M. Anjanappa, M. Corden, A. Green, D. Roberts, P. Hoskin, A. McWilliam, A. Choudhury, Sarcopenia in cancer: Risking more than muscle loss, Technical Innovations & Patient Support in Radiation Oncology 16 (2020) 50–57, https://doi.org/10.1016/j.tipsro.2020.10.001.
[4] X. Shu, T. Lin, H. Wang, Y. Zhao, T. Jiang, X. Peng, J. Yue, Diagnosis, prevalence, and mortality of sarcopenia in dialysis patients: a systematic review and meta-analysis, Journal of Cachexia, Sarcopenia and Muscle 13 (2022) 145–158, https://doi.org/10.1002/jcsm.12890.
[5] M. Gui, L. Lv, S. Hu, L. Qin, C. Wang, Sarcopenia in Parkinson's disease: from pathogenesis to interventions, Metabolism 169 (2025) 156272, https://doi.org/10.1016/j.metabol.2025.156272.
[6] X. Li, J. He, Q. Sun, The prevalence and effects of sarcopenia in patients with metabolic dysfunction-associated steatotic liver disease (MASLD): A systematic review and meta-analysis, Clinical Nutrition 43 (2024) 2005–2016, https://doi.org/10.1016/j.clnu.2024.07.006.
[7] L. Feng, Q. Gao, K. Hu, M. Wu, Z. Wang, F. Chen, F. Mei, L. Zhao, B. Ma, Prevalence and Risk Factors of Sarcopenia in Patients With Diabetes: A Meta-analysis, The Journal of Clinical Endocrinology & Metabolism 107 (2022) 1470–1483, https://doi.org/10.1210/clinem/dgab884.
[8] C.J. Christian, G.M. Benian, Animal models of sarcopenia, Aging Cell 19 (2020) e13223, https://doi.org/10.1111/acel.13223.
[9] P. Wiedmer, T. Jung, J.P. Castro, L.C.D. Pomatto, P.Y. Sun, K.J.A. Davies, T. Grune, Sarcopenia – Molecular mechanisms and open questions, Ageing Research Reviews 65 (2021) 101200, https://doi.org/10.1016/j.arr.2020.101200.
[10] Sarcopenia: no consensus, no diagnostic criteria, and no approved indication—How did we get here? | GeroScience, (n.d.) (accessed June 20, https://link.springer.com/article/10.1007/s11357-023-01016-9, 2025 (accessed June 20).
[11] S. Srivastava, S. Srivastava, Biological activity of Quinazoline: A Review, 6 (2015).
[12] J.B. Koepfli, J.A. Brockman Jr, J. Moffat, THE STRUCTURE OF FEBRIFUGINE AND ISOFEBRIFUGINE1, ACS Publications (2002), https://doi.org/10.1021/ja01163a555.
[13] V. Alagarsamy, K. Chitra, G. Saravanan, V.R. Solomon, M.T. Sulthana, B. Narendhar, An overview of quinazolines: Pharmacological significance and recent developments, European Journal of Medicinal Chemistry 151 (2018) 628–685, https://doi.org/10.1016/j.ejmech.2018.03.076.
[14] A.B. Ceyhan, M. Ozcan, W. Kim, X. Li, O. Altay, C. Zhang, A. Mardinoglu, Novel drug targets and molecular mechanisms for sarcopenia based on systems biology, Biomedicine & Pharmacotherapy 176 (2024) 116920.
[15] G.M. Sheldrick, SHELXT – Integrated space-group and crystal-structure determination, Acta Cryst A 71 (2015) 3–8, https://doi.org/10.1107/S2053273314026370.
[16] G.M. Sheldrick, Crystal structure refinement with SHELXL, Acta Cryst C 71 (2015) 3–8, https://doi.org/10.1107/S2053229614024218.
[17] O.V. Dolomanov, L.J. Bourhis, R.J. Gildea, J.a.K. Howard, H. Puschmann, OLEX2: a complete structure solution, refinement and analysis program, J Appl Cryst 42 (2009) 339–341, https://doi.org/10.1107/S0021889808042726.
[18] Schrödinger Release 2023-3, Schrödinger, LLC, New York, NY (2023), (n.d.).
[19] S. Release, 2: Protein Preparation Wizard; Epik, Schrödinger, LLC, NY, 2023; Impact, Schrödinger, LLC, NY, NY: Prime, Schrödinger, LLC (2023).
[20] Schrödinger Release 2023-3, LigPrep, Schrödinger, LLC, New York, NY (2023, (n.d.).
[21] V. GaussView, 6.1, R. Dennington, TA Keith, JM Millam, Semichem Inc (2016).
[22] M. Frisch, G.W. Trucks, H.B. Schlegel, G.E. Scuseria, M.A. Robb, J.R. Cheeseman, G. Scalmani, V. Barone, B. Mennucci, G.A. Petersson, gaussian 09, Gaussian, Inc., Wallingford CT 121 (2009) 150–166.
[23] S.F. Boys, F. Bernardi, The calculation of small molecular interactions by the differences of separate total energies. Some procedures with reduced errors, Molecular Physics 19 (1970) 553–566, https://doi.org/10.1080/00268977000101561.
[24] C. Lefebvre, H. Khartabil, J. Boisson, J. Contreras-García, J. Piquemal, E. Hénon, The Independent Gradient Model: A New Approach for Probing Strong and Weak Interactions in Molecules from Wave Function Calculations, ChemPhysChem 19 (2018) 724–735, https://doi.org/10.1002/cphc.201701325.
[25] E. Bartashevich, S. Mukhitdinova, I. Yushina, V. Tsirelson, Electronic criterion for categorizing the chalcogen and halogen bonds: sulfur–iodine interactions in crystals, Structural Science 75 (2019) 117–126.

[26] T. Lu, F. Chen, Multiwfn: A multifunctional wavefunction analyzer, J Comput Chem 33 (2012) 580–592, https://doi.org/10.1002/jcc.22885.
[27] W. Humphrey, A. Dalke, K. Schulten, VMD: visual molecular dynamics, Journal of Molecular Graphics 14 (1996) 33–38.
[28] S. Ashraf, S. Iqbal, J. Sebhaoui, M. Ozcan, W. Kim, B. Belmen, G. Yeşilyurt, E. Hanashalshahaby, C. Zhang, M. Uhlen, Synthesis, spectroscopic characterization, DFT and molecular docking of N-(3-cyano-4, 5, 6, 7-tetrahydrobenzo [b] thiophen-2-yl) naphthalene-1-sulfonamide derivatives, Journal of Molecular Structure 1312 (2024) 138470.
[29] M. Sanam, S. Ashraf, M. Saeed, A. Khalid, A.N. Abdalla, U. Qureshi, Z. Ul-Haq, Cebranopadol: An Assessment for Its Biased Activation Potential at the Mu Opioid Receptor by DFT, Molecular Docking and Molecular Dynamic Simulation Studies, ChemistrySelect 8 (2023) e202302090, https://doi.org/10.1002/slct.202302090.